On Vibration Suppression and Energy Dissipation Using Tuned Mass Particle Damper

Shilong Li
Department of Mechanical Engineering,
University of Connecticut,
191 Auditorium Road, Unit 3139,
Storrs, CT 06269

J. Tang[1]
Professor
Department of Mechanical Engineering,
University of Connecticut,
191 Auditorium Road, Unit 3139,
Storrs, CT 06269
e-mail: jtang@engr.uconn.edu

Particle damping has the promising potential for attenuating unwanted vibrations in harsh environments especially under high temperatures where conventional damping materials would not be functional. Nevertheless, a limitation of simple particle damper (PD) configuration is that the damping effect is insignificant if the local displacement/acceleration is low. In this research, we investigate the performance of a tuned mass particle damper (TMPD) in which the particle damping mechanism is integrated into a tuned mass damper (TMD) configuration. The essential idea is to combine the respective advantages of these two damping concepts and in particular to utilize the tuned mass damper configuration as a motion magnifier to amplify the energy dissipation capability of particle damper when the local displacement/acceleration of the host structure is low. We formulate a first-principle-based dynamic model of the integrated system and analyze the particle motion by using the discrete element method (DEM). We perform systematic parametric studies to elucidate the damping effect and energy dissipation mechanism of a TMPD. We demonstrate that a TMPD can provide significant vibration suppression capability, essentially outperforming conventional particle damper.
[DOI: 10.1115/1.4034777]

Keywords: particle damper, tuned mass damper, tuned mass particle damper, discrete element method, energy dissipation, vibration suppression

1 Introduction

Passive damping devices are widely used to protect the primary structures from sudden shocks and/or persistent excitations. Although viscoelastic materials and fluid dampers are commonly implemented [1], one major drawback of such devices is that their performance is sensitive to ambient environment and generally can only function properly under moderate temperatures. Alternatively, particle damper, owing to the advantage of being robust with respect to extreme temperatures, has attracted broad interest [2–6]. The underlying principle of particle damper is the energy absorption and dissipation through the collision and the friction between the particles and the hosting enclosure and among the particles, leading to the attenuation of vibration. While particle damper is simple in concept, its behavior is very complicated as the energy dissipation mechanism is highly nonlinear. A few analytical and experimental studies have been conducted to analyze the particle damping mechanism [7–9]. There have also been continuous efforts [10–12] on developing efficient numerical methods to quantify the particle damping effect using such as the DEM [13], which keeps track of the motion of all the particles.

The effectiveness of a particle damper depends on many parameters, such as size, shape and material of the particles, local excitation level, and geometry of the enclosure [14]. Usually, a particle damper is attached to region where the level of displacement/acceleration is relatively high. The motions of vertically vibrating particles in an enclosure may undergo three stages, i.e., solid, convective, and gaslike regimes [15,16]. When the acceleration level is lower than gravity, particles are in the solid stage as they are locked and move together with the enclosure, which results in little damping effect. As acceleration increases, some particles inside the enclosure start to slide over and collide with each other, dissipating energy via the frictions and collisions. At this stage, the particles act like fluid with convections inside the enclosure [15]. Further increase of acceleration level then yields gaslike motion of particles, especially for dilute or moderately dense particle systems. It is reported that higher damping capacity may occur in the fluidlike regime since both the collision and friction dominate the motions of particles [9,17]. For cases where local displacements/accelerations throughout the structure are low, the performance of particle damper would be limited.

There exists a well-known passive damping design concept, the TMD [18]. In such a concept, additional mechanical components with spring, mass, and damper elements are added to the structure to form an absorber. In the classical design, the absorber stiffness is tuned such that the absorber natural frequency matches with the excitation frequency of concern, e.g., the fundamental frequency of the host structure, and the damping coefficient is properly tuned subsequently to maximize the energy dissipation over the interested frequency range. There have been a series of studies on TMDs with varying levels of design complexity [19–21]. It is worth noting that the damping involved in the TMDs is usually realized by using viscous or hysteretic materials [19] that, again, may be subjected to limitation in severe environments especially under high temperatures.

Here, we consider a TMPD shown in Fig. 1, which combines a beam-type tuned mass damper and a particle damper. The additional beam essentially serves as the stiffness element of a TMD,

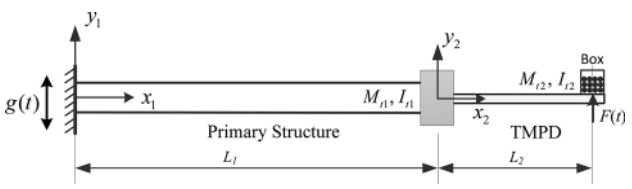

Fig. 1 Schematic of primary beam structure integrated with the TMPD

[1]Corresponding author.

Contributed by the Technical Committee on Vibration and Sound of ASME for publication in the Journal of Vibration and Acoustics. Manuscript received March 21, 2016; final manuscript received September 14, 2016; published online October 27, 2016. Assoc. Editor: Mahmoud Hussein.

whereas the mass of the TMD is replaced by a particle damper which at the same time also provides energy dissipation capability through particle motion. To avoid potential limitation of traditional TMDs under severe environment, there is no other damping element involved. In this configuration, the additional beam, in combination with the particle damper mass, can play the role of motion magnifier [22]. To facilitate this, the TMPD is connected to a rigid block attached to the host beam. The host beam together with the rigid block modeled as tip mass is considered as the primary structure. The basic tuning criterion is to tune the natural frequency of the TMPD to be equal to that of the primary structure. Before taking into consideration its damping ability, a TMPD is simply an undamped absorber. The magnified level of displacement/acceleration of the particle damper enclosure in a TMPD, meanwhile, can yield increased energy dissipation capability especially when the host structure has low displacement/acceleration levels, since it can absorb significant portion of the vibratory energy. There have been, however, very limited studies concerning the TMPD analysis. Yao et al. [17] presented an approximate model through simplifying the host structure and the TMPD into a three degrees-of-freedom (DOFs) system, where the TMPD was characterized by using viscous damping coefficient and equivalent stiffness and mass coefficients extracted from certain operating conditions.

Owing to the nature of particle motions involved, a TMPD is inherently nonlinear. The intention of this research is to develop a systematic, first-principle-based analysis of this damping mechanism to elucidate the parametric influences. As shown in Fig. 1, a beam with tip mass is adopted as the host structure. A coupled algorithm is formulated that allows the integrated analysis of the host structure and the TMPD. Three-dimensional DEM is implemented to simulate the particle motion characteristics. In order to validate the accuracy of the model and the numerical analysis, experimental investigations on the TMPD and the traditional PD are conducted under different base excitations. Then, using the model developed, we quantitatively evaluate the difference in energy dissipation efficacies of the TMPD and PD and also conduct parametric investigations on enclosure dimensions and volumetric filling ratios, aiming at providing design guidelines for TMPD.

2 Formulation of Coupled Analysis of TMPD and Host Structure

In this section, we formulate a dynamic model for a TMPD that is integrated with a primary structure. As shown in Fig. 1, the host beam is cantilevered and has length L_1. The TMPD consists of a beam with length L_2 that is connected rigidly with the host beam at its tip rigid block, and a box enclosed with particles that is attached to the tip of the TMPD beam. The host beam and the TMPD beam form a segmented beam structure, while the particles move vertically inside the box/enclosure. We first outline the modal analysis of the segmented beam followed by a forced response expression for beam vibration. We then present the discrete element method to be used for particle motion simulation. These two motions are finally coupled together based on the compatibility conditions of impact/friction and displacement/velocity between the segmented beam and the particles at the box location.

2.1 Vibration of Segmented Beam

2.1.1 Segmented Beam Modal Analysis. Since the connection between them is rigid, the host beam and the TMPD beam are considered as one single beam with two segments associated with the respective coordinates x_1 and x_2, as shown in Fig. 1. Each segment is uniform, with Young's modulus, mass density, area moment of inertia, and cross-sectional area as E_n, ρ_n, I_n, and A_n ($n = 1, 2$). Assume negligible beam damping, the free vibration of the segmented beam is described as [23]

$$E_n I_n w''''(x_n, t) + \rho_n A_n \ddot{w}(x_n, t) = 0, \quad n = 1, 2 \tag{1}$$

where $w(x_n, t)$ denotes the vertical displacement of the beam at location x_n on segment n. For the above equation, the standard separation of variables approach can be used, which yields the expression of the rth normalized mode shape $\phi_{rn}(x_n)$ ($n = 1, 2$)

$$\phi_{rn}(x_n) = a_{n1}\cos(\beta_{rn}x_n) + a_{n2}\sin(\beta_{rn}x_n) + a_{n3}\cos h(\beta_{rn}x_n) + a_{n4}\sin h(\beta_{rn}x_n),\ n = 1, 2 \tag{2}$$

where β_{rn} is related to the natural frequency ω_{rn} as

$$\omega_{rn} = \beta_{rn}^2\sqrt{\frac{E_n I_n}{\rho_n A_n}} \tag{3}$$

Apparently, as the two segments are connected together, we must have

$$\beta_{r1}^2\sqrt{\frac{E_1 I_1}{\rho_1 A_1}} = \beta_{r2}^2\sqrt{\frac{E_2 I_2}{\rho_2 A_2}} \tag{4}$$

The mode shapes and the natural frequencies are determined through the boundary conditions at $x_1 = 0$ and $x_2 = L_2$ as well as the compatibility conditions at $x_1 = L_1$ and $x_2 = 0$, i.e.,

$$\phi_{r1}(0) = 0 \tag{5a}$$

$$\phi'_{r1}(0) = 0 \tag{5b}$$

$$E_1 I_1 \phi'''_{r1}(L_1) - E_2 I_2 \phi'''_{r2}(0) = -\omega_{r1}^2 M_{t1}\phi_{r1}(L_1) \tag{5c}$$

$$E_1 I_1 \phi''_{r1}(L_1) - E_2 I_2 \phi''_{r2}(0) = \omega_{r1}^2 I_{t1}\phi'_{r1}(L_1) \tag{5d}$$

$$\phi_{r1}(L_1) = \phi_{r2}(0) \tag{5e}$$

$$\phi'_{r1}(L_1) = \phi'_{r2}(0) \tag{5f}$$

$$E_2 I_2 \phi'''_{r2}(L_2) = -\omega_{r2}^2 M_{t2}\phi_{r2}(L_2) \tag{5g}$$

$$E_2 I_2 \phi''_{r2}(L_2) = \omega_{r2}^2 I_{t2}\phi_{r2}(L_2) \tag{5h}$$

Here, Eqs. (5*a*), (5*b*), (5*e*), and (5*f*) simply represent the displacement and slope conditions, Eqs. (5*c*) and (5*d*) indicate that the shear and moment at the end of the host beam are balanced by the inertia effects of the rigid block at its tip, and Eqs. (5*g*) and (5*h*) indicate that shear and moment at the end of the TMPD beam are balanced by the inertia effects of the particle enclosure. In these equations, M_{t1} and M_{t2} are the masses of the rigid block and the particle enclosure, and I_{t1} and I_{t2} are their moments of inertia. The mode shape solved for the respective beam segment can be written uniformly as [23]

$$\phi_r(x) = \phi_{r1}(x)H(L_1 - x) + \phi_{r2}(x - L_1)H(x - L_1) \tag{6}$$

where x now denotes the coordinate of the entire structure, and H is the Heaviside function.

A comparison of the natural frequencies and mode shapes solved analytically based on the above formulation and that solved by finite-element method is shown in Fig. 2. As can be seen, the results match well. The parameters used will be explained in full detail in Sec. 3. In this research, the analytical mode will be used in beam discretization and the subsequent vibration analysis.

2.1.2 Beam Vibration Under Base Excitation and TMPD Effect. The primary structure with TMPD as shown in Fig. 1 is subjected to base excitation, $\ddot{g}(t) = G\sin(\omega t)$, where G is the

acceleration amplitude, and ω is the excitation frequency, which is consistent with the experimental condition. Thus, the absolute transversal motion can be expressed as

$$w(x,t) = w_{\text{rel}}(x,t) + g(t) \tag{7}$$

where $w_{\text{rel}}(x,t)$ is the transversal displacement relative to the clamped end of the host beam, and $g(t)$ is the base motion. Recall the modal analysis in Sec. 2.1.1. We apply the assumed mode method and let the relative transversal displacement be expressed as

$$w_{\text{rel}}(x,t) = \sum_{r=1}^{m} \phi_r(x)\eta_r(t) \tag{8}$$

where $\eta_r(t)$ is the rth generalized coordinate, and m is the number of modes used. The force due to the particles in the enclosure, assumed to act at the center of the bottom of the enclosure, is denoted as $F(t)\delta(x - L_1 - L_2)$ (Fig. 1), where δ is the usual Kronecker delta function. The beam vibration under base excitation and TMPD effect is then described by

$$\sum_{r=1}^{m} \frac{d^2}{dx^2}\left[E(x)I(x)\frac{d^2\phi_r(x)}{dx^2}\right]\eta_r(t) + \sum_{r=1}^{m} \rho(x)A(x)\phi_r(x)\frac{d^2\eta_r(t)}{dt^2}(t) = F(t)\delta(x - L_1 - L_2) - \rho(x)A(x)\ddot{g} \tag{9}$$

Multiplying Eq. (9) by an arbitrary mode shape $\phi_s(x)$ and integrating over the entire length of the beam, recalling the mode orthogonality, we can obtain

$$\ddot{\eta}_s(t) + 2\zeta_s\omega_s\dot{\eta}(t) + \omega_s^2\eta(t) = N_s(t) \tag{10}$$

where

$$N_s(t) = F(t)\phi_s(L_1 + L_2) - \int_0^{L_1} \rho_1 A_1 \ddot{g}(t)\phi_s(x)dx - \int_{L_1}^{L_2} \rho_2 A_2 \ddot{g}(t)\phi_s(x)dx - M_{t1}\ddot{g}(t)\phi_s(L_1) - M_{t2}\ddot{g}(t)\phi_s(L_1 + L_2) \tag{11}$$

In this research, we assume that the beam is subjected to proportional damping and ζ_s is the modal damping ratio. The time-dependent effect of the particle damper, $F(t)$ shown in Eq. (11), will be determined in Sec. 2.

2.2 Vibration Analysis of Particles Via Discrete Element Method. This section outlines how the particles in the enclosure of the TMPD are analyzed. Here, we adopt the DEM [12,13], which tracks the trajectory of each particle (i.e., discrete element) incrementally based on first principle. The forces among particles are based on the contact behaviors. The damper enclosure interacts with the host beam through the force and displacement compatibility between the particles and the beam.

2.2.1 Contact Mechanics Model. An important aspect of modeling particle motion is the selection of the contact mechanics model. Two particles are in contact and contact forces occur, when the distance between the centers of two particles is less than the summation of their radii. Two particles are allowed to overlap in order to facilitate the calculation of contact forces based on the model using spring, dashpot, and slider in the normal and tangential direction as illustrated in Fig. 3 [24]. A number of experimental and numerical studies have demonstrated that a nonlinear force–displacement model can effectively describe the contact

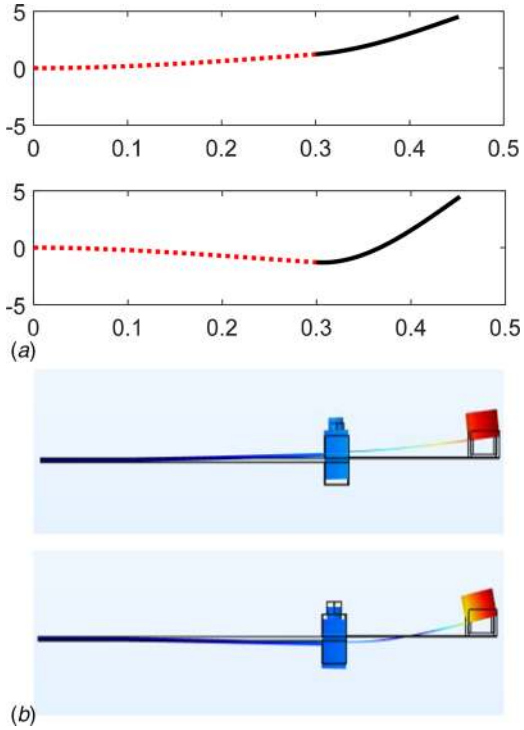

Fig. 2 First two mode shapes of the segmented beam: (*a*) analytical result ($f_1 = 5.93$ Hz and $f_2 = 10.30$ Hz) and (*b*) finite element result ($f_1 = 5.99$ Hz and $f_2 = 10.47$ Hz)

mechanics [25,26]. In this study, the nonlinear contact model suggested by Tsuji et al. [24] is implemented.

As shown in Fig. 3, the contact force acting on particle i by another particle j or the wall has the normal component $\mathbf{f}_{nij}$ and the tangential component $\mathbf{f}_{tij}$. The normal component can be modeled as the summation of the spring force through the Hertzian contact theory and the damping force [24], i.e.,

$$\mathbf{f}_{nij} = -(k_n\delta_{nij}^{3/2} + \eta_{nij}\mathbf{v}_{ij}\mathbf{n}_{ij})\mathbf{n}_{ij} \tag{12}$$

where $\mathbf{v}_{ij} = \mathbf{v}_i - \mathbf{v}_j$ is the velocity of particle i relative to particle j, δ_{nij} is the normal relative displacement between these two particles, k_n is the stiffness of the spring, η_{nij} is the normal damping coefficient, and $\mathbf{n}_{ij}$ is the unit vector from the center of particle i to that of particle j. In the case of contact between two particles, the normal displacement δ_{nij} can be expressed as

$$\delta_{nij} = r_i + r_j - |\mathbf{p}_j - \mathbf{p}_i| \tag{13}$$

where r_i, $\mathbf{p}_i$, and r_j, $\mathbf{p}_j$ are the radius and the center position of particles i and j, respectively. The spring stiffness k_n can be expressed as, based on the Hertzian contact theory [27]

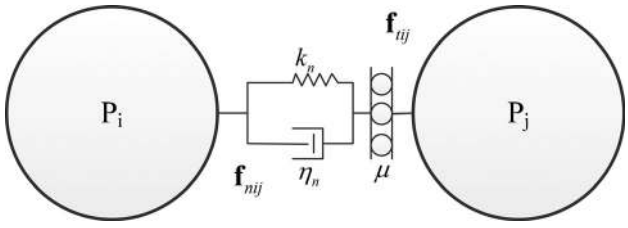

Fig. 3 Sketch of spring, dashpot, and slider model for contact force

$$k_n = \frac{4}{3}\sqrt{\frac{r_i r_j}{r_i + r_j}}\frac{E_i E_j}{\left(1-\nu_j^2\right)E_i + \left(1-\nu_i^2\right)E_j} \tag{14}$$

where E and ν are the Young's modulus and Poisson's ratio of the particle, respectively. In the case of contact between a particle and the enclosure wall, the stiffness is

$$k_n = \frac{4\sqrt{r_i}}{3}\frac{E_i E_w}{\left(1-\nu_w^2\right)E_i + \left(1-\nu_i^2\right)E_w} \tag{15}$$

where E_w and ν_w are the Young's modulus and Poisson's ratio of the enclosure wall, respectively. As suggested by Tsuji et al. [24], the damping coefficient takes the following form:

$$\eta_{nij} = \alpha\sqrt{m_i k_n}\delta_{nij}^{1/4} \tag{16}$$

where m_i is the mass of particle, and α is a constant coefficient related to the coefficient of restitution.

The tangential component of the contact force can be decided by using Coulomb's friction [3]

$$\mathbf{f}_{tij} = -\mu|\mathbf{f}_{nij}|\mathbf{v}_{tij}/|\mathbf{v}_{tij}| \tag{17}$$

In Eq. (17), μ is the friction coefficient, and $\mathbf{v}_{tij}$ is the relative velocity at the contact point along the tangential direction, i.e.,

$$\mathbf{v}_{tij} = \mathbf{v}_{ij} - (\mathbf{v}_{ij}\mathbf{n})\mathbf{n} + r(\boldsymbol{\omega}_i + \boldsymbol{\omega}_j) \times \mathbf{n} \tag{18}$$

where $\boldsymbol{\omega}_i$ and $\boldsymbol{\omega}_j$ are the angular velocities of particles i and j, respectively.

2.2.2 Particle Motion Equations. An individual particle has two types of motion: translational motion caused by the contact and gravitational forces and rotational motion induced by the contact forces only. Usually, a particle i is in contact with many other particles or the enclosure wall at the same time. Therefore, its motion is characterized by the following equations [12,24]:

$$m_i\ddot{\mathbf{p}}_i = \sum_j(\mathbf{f}_{nij} + \mathbf{f}_{tij}) - m_i\mathbf{g} \tag{19a}$$

$$I_i\ddot{\theta}_i = \sum_j(r\mathbf{n}_{ij} \times \mathbf{f}_{tij}) \tag{19b}$$

where $\mathbf{p}_i$, θ_i, m_i, and I_i are, respectively, the position vector, the angular displacement vector, the mass, and the moment of inertia of particle i, and $\mathbf{g}$ is the gravitational acceleration vector. The finite difference format can be employed to express the translational and angular velocities as

$$\dot{\mathbf{p}}_i^{(t+\Delta t/2)} = \dot{\mathbf{p}}_i^{(t-\Delta t/2)} + \ddot{\mathbf{p}}_i^t\Delta t \tag{20a}$$

$$\dot{\theta}_i^{(t+\Delta t/2)} = \dot{\theta}_i^{(t-\Delta t/2)} + \ddot{\theta}_i^t\Delta t \tag{20b}$$

The translational and angular positions of particle i at time $t + \Delta t$ are

$$\mathbf{p}_i^{(t+\Delta t)} = \mathbf{p}_i^{(t)} + \dot{\mathbf{p}}_i^{(t+\Delta t/2)}\Delta t \tag{21a}$$

$$\theta_i^{(t+\Delta t)} = \theta_i^{(t)} + \dot{\theta}_i^{(t+\Delta t/2)}\Delta t \tag{21b}$$

In order to improve the computational efficiency of classical DEM approach, a Verlet table [28] combined with linked cell method [12] is applied to enhance the contact detection which is the most time-consuming step. An adaptive strategy for updating the Verlet table is also employed to further boost the contact detection efficiency.

2.3 Coupled Analysis of Beam and TMPD Through Iterative Computation in Time-Domain. We can now combine beam vibration analysis with particle motion analysis. Recall Eq. (10) where the beam vibration is discretized and converted to the modal space. To account for the dynamic coupling between the beam and the TMPD, here we use the first two modes of the beam with two segments for discretization. We use time-marching scheme in numerical analysis. As the beam vibrates, we compute the physical response as the summation of the first two modal responses subjected to the particle damping effect as well as the base excitation. The beam motion in turn causes impact and friction to the particles through the particle–enclosure interaction. We then use time-marching finite difference again on particle motion analysis. This procedure repeats throughout the entire simulation period. The flowchart is shown in Fig. 4.

3 Experimental Validation

3.1 Experimental Setup. To validate the numerical analysis and to explore the vibration suppression performance of TMPD, a series of experiments are conducted. Obviously, the selection of TMPD parameters plays an important role. It is worth noting that the intent of this research is to elucidate the energy distribution/dissipation of a primary structure integrated with a TMPD rather than to provide a rigorous optimization scheme which will be a possible future research subject for a specific application. Therefore, the TMPD parameters are selected in a heuristic manner, mainly based on the undamped vibration absorber concept (or a TMD without the damping element). That is, for a given host beam and its tip mass that form the primary structure, we tune the natural frequency of the TMPD to be equal to that of the primary structure, such that the TMPD will be able to absorb significant amount of energy from the primary structure at its resonant frequency. The natural frequency of the TMPD is computed based upon the enclosure mass and the TMPD beam stiffness (under cantilever condition). We exclude the particle mass when computing the natural frequency of the TMPD, because, as will be seen later, with the motion magnifying effect due to TMPD the particles become more separated with the enclosure floor. A similar treatment was suggested by Zhou et al. [29] on the design of an

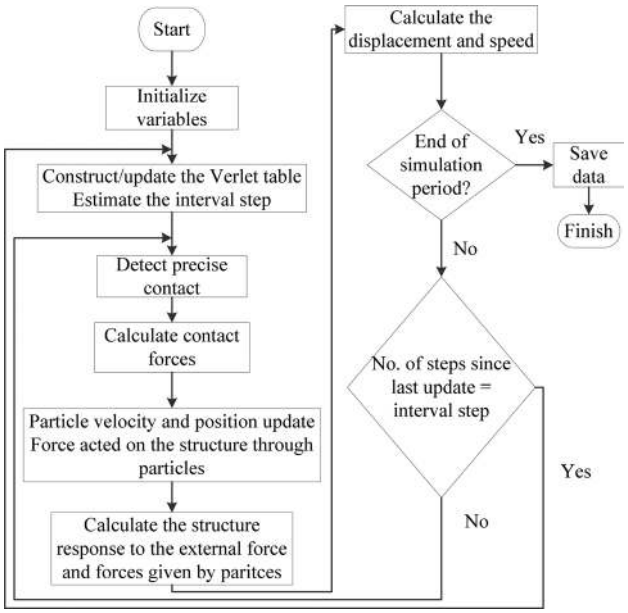

Fig. 4 Flowchart for the iterative numerical procedure

Table 1 Dimensions of primary beam structure with TMPD

Beam	Length, L (mm)	Width, b (mm)	Thickness, h (mm)	Tip mass M_{t1} and enclosure mass M_{t2} (g)
Primary beam	300.0	38.1	3.175	286.16
TMPD	150.0	25.0	0.810	23.240

improved piezoelectric energy harvester. Both the host beam and the TMPD beam are made of the same type of aluminum with density 2700 kg/m^3, Young's modulus 68.9 GPa, and Poisson's ratio 0.33. The parameters of the beams involved in the experiment are listed in Table 1. The TMPD enclosure is made of cast aluminum, and the related parameters are listed in Table 2. Acrylic resin spheres are used as particles involved in TMPD, and their properties are listed in Table 2 as well. The experimental setup is shown in Fig. 5. The mass of the accelerometer mounted on the tip of the primary structure is accounted for in both experiment and numerical analyses.

3.2 Correlation of Experimental and Numerical Results. Four different configurations are studied experimentally as shown in Fig. 6: (1) primary structure attached with the empty enclosure (serving as the baseline); (2) primary structure with a conventional PD attached to its tip; (3) primary structure with TMPD configuration but without particles (i.e., an undamped vibration absorber tuned to the primary structure's natural frequency); and (4) primary structure integrated with TMPD (particles are filled into the enclosure). Tip accelerations of the primary structure under sinusoidal base movement with constant amplitude are measured. The vibration shaker excites the structure in swept sine mode in the frequency range of 4–12 Hz (which covers the first and second natural frequencies of the integrated system). In order to keep the amplitude of excitation acceleration constant, the input voltage to the shaker at each frequency point is adjusted based on the measurement of the accelerometer attached to the base. Since the response behavior of the structure with particles is generally nonlinear [12], the root-mean-square (RMS) value of the primary system acceleration versus the excitation frequency is employed to quantify the damping effect. Our main objective is to compare TMPD (configuration (4)) with conventional PD (configuration (2)). Because our hypothesis is that the TMPD can potentially magnify the particle motions to amplify the damping effect, we also compare TMPD with configuration (3) in which no particles are present. Indeed, as mentioned, configuration (3) is an undamped absorber targeting at the natural frequency of the primary structure. To facilitate all these comparisons, we also analyze configuration (1) which can be considered as the baseline, i.e., having neither vibration absorbing nor energy dissipation mechanisms other than its inherent structural damping.

Figures 7–9 show the frequency responses of the primary structure under these four configurations obtained from the experimental measurements and the numerical simulations. The base excitation levels are 0.15 m/s^2, 0.25 m/s^2, and 0.3 m/s^2, respectively. Note that the accelerometer measures the absolute value, which is the sum of the relative acceleration and the base

Table 2 Parameters of enclosure and particles

Enclosure		Particles	
Length	34.04 mm	Particle–particle normal stiffness	$2.5 \times 10^9 \sqrt{r/2}$ N/m$^{3/2}$
Width	24.64 mm	Particle–wall normal stiffness	$4.5 \times 10^9 \sqrt{r}$ N/m$^{3/2}$
Height	19.30 mm	Coefficient of restitution	0.89
Density	2700 kg/m^3	Coefficient of friction	0.52
Young's modulus	70 GPa	Particle diameter ($2r$)	3.2 mm
		Particle number	210

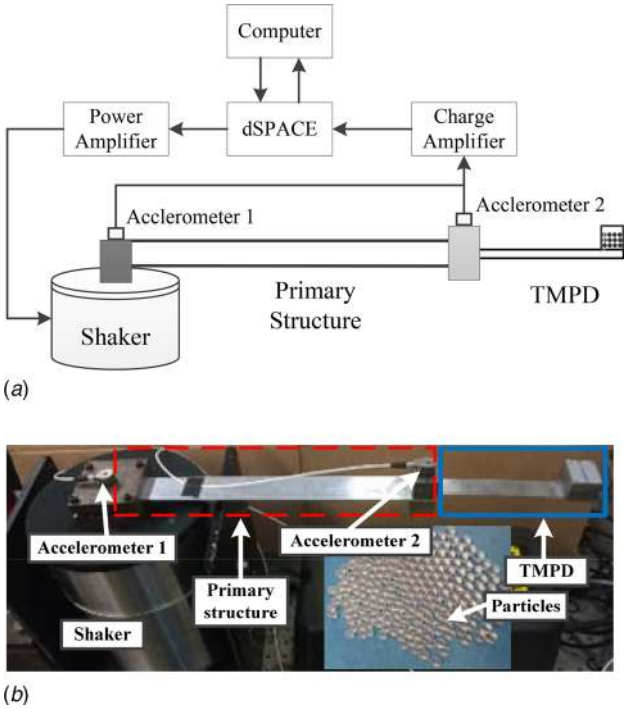

Fig. 5 Experimental setup: (*a*) schematic of the experiment and (*b*) prototype

acceleration. All the simulations are run for 20 s so the transients die out, and the initial positions of particles are set to be distributed randomly to represent realistic situations. As can be seen, for the four cases, the overall frequency responses and resonant frequencies calculated match closely with the experimental results, which demonstrates the validity and accuracy of the model that we have developed. For example, the errors of the first and second resonant frequencies of the undamped baseline are 1.26% and 2.62%, respectively. In both experimental measurements and numerical simulations, we can observe the phenomena of frequency shifts, i.e., the peak response frequencies of the system with particles shifting toward those without particles, as the excitation level increases. This is similar to what is observed in conventional PD, which is caused by particles spending more time being separated from the enclosure under higher excitation levels [9]. The small errors of the numerical results (in terms of resonant frequencies) are possibly due to the slight mismatch between the

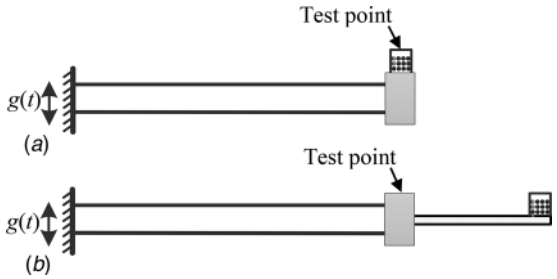

Fig. 6 Schematics of (*a*) conventional PD and (*b*) TMPD

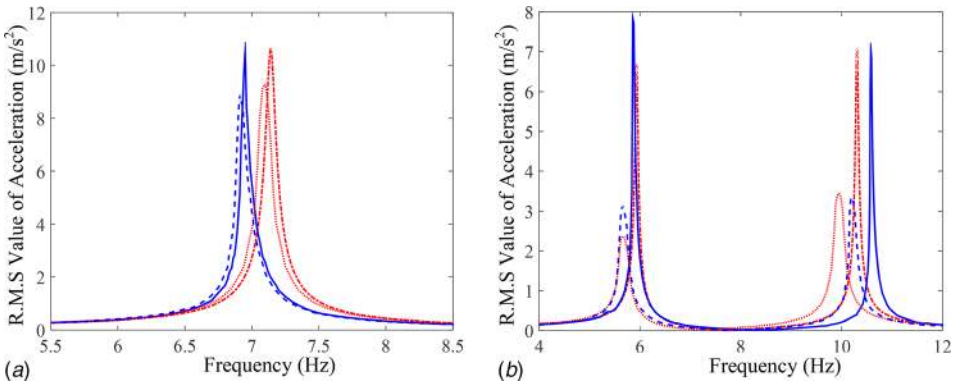

Fig. 7 Frequency responses when $G = 0.15\,\text{m/s}^2$. ——: No damper (experiment); – · – · –: no damper (simulation); – – –: with damper (experiment); and · · ·: with damper (simulation). (*a*) PD and (*b*) TMPD.

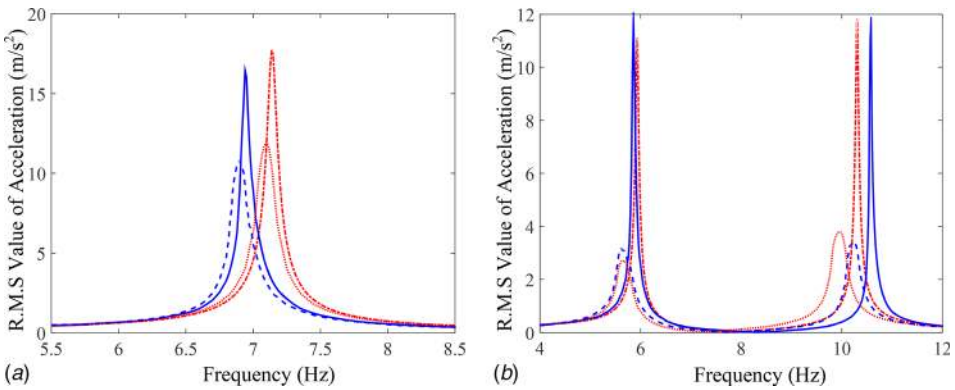

Fig. 8 Frequency responses when $G = 0.25\,\text{m/s}^2$. ——: No damper (experiment); – · – · –: no damper (simulation); – – –: with damper (experiment); and · · ·: with damper (simulation). (*a*) PD and (*b*) TMPD.

mathematical idealization and the actual boundary condition and other parametric uncertainties.

All the results indicate that the TMPD has the vibration suppression ability among the configurations studied under assigned excitation levels and frequencies. Figure 7 shows that, when the external excitation level is low, the vibration suppression performance of the undamped absorber is actually better than the conventional PD due to the fact that the PD does not exhibit significant damping ability (i.e., local acceleration less than the gravity, causing little particle motions). It is worth noting that, under base excitation, the excitation forces applied to the structure as shown in Eq. (11) are mainly produced by the inertia effects of the beams and the tip masses. Hence, under the same base excitation acceleration level, the overall excitation forces applied to the structure in configurations (1) and (2) may be less than those in configurations (3) and (4). A more comprehensive numerical analysis will be conducted in Sec. 4.

4 Simulation-Based Parametric Analysis

As the validity of the mathematical model is confirmed in Sec. 3, in this section using numerical simulations we carry out several parametric analyses to elucidate the vibration suppression and energy dissipation mechanisms. We report the energy dissipation

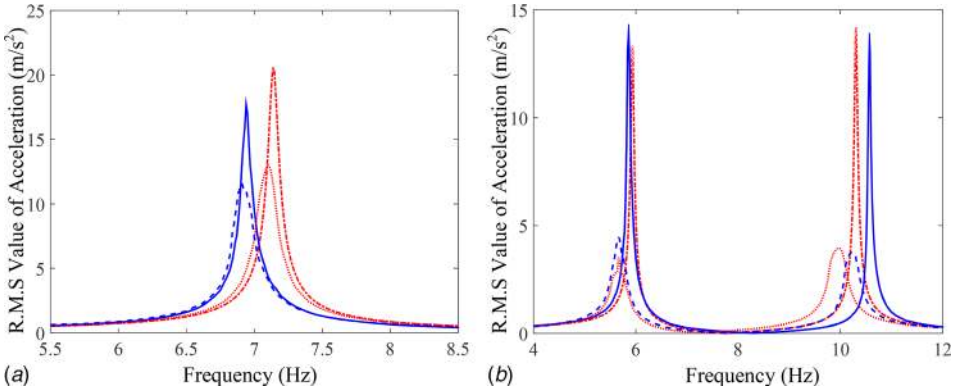

Fig. 9 Frequency responses when $G = 0.30\,\text{m/s}^2$. ——: No damper (experiment); – · – · –: no damper (simulation); – – –: with damper (experiment); and · · ·: with damper (simulation). (*a*) PD and (*b*) TMPD.

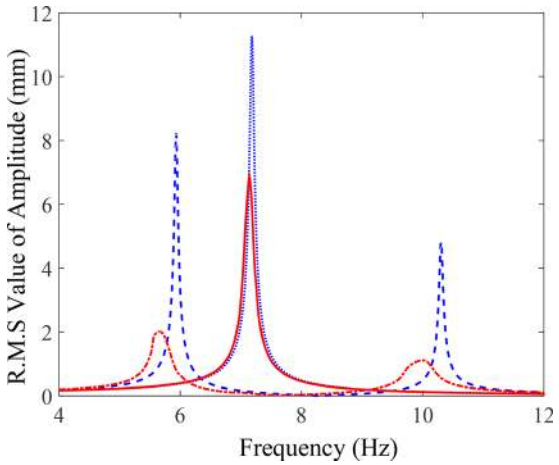

Fig. 10 Comparison of frequency responses of four configurations when $A = 0.11$ N. – – –: Configuration 1 (baseline); ——: configuration 2 (PD); – – –: configuration 3 (undamped absorber); and – · – · –: configuration 4 (TMPD)

characteristics of particle motions which may not be easily observed experimentally.

4.1 TMPD Vibration Suppression Capability. Particle damping is generally nonlinear and its performance depends heavily on a number of parameters, including the excitation amplitude and frequency. Here in order to more fairly compare the vibration suppression capability of TMPD with that of conventional PD under identical excitations, in the numerical model we now apply, to all four configurations mentioned, an identical harmonic excitation $G(t) = A\sin(2\pi ft)$ at the right end of the primary structure. A and f are the excitation amplitude and frequency, respectively. Other parameters remain unchanged (as shown in Tables 1 and 2).

We start from analyzing the vibration response reduction. Figure 10 shows the frequency response plots for the four different configurations under an excitation level $A = 0.11$ N. From the figure, we can observe that the maximum amplitude of the original structure is 11.25 mm, which is reduced to 6.89 mm by the conventional PD, i.e., a 38.76% reduction. With the TMPD, the maximum amplitude is reduced to 2.01 mm, i.e., an 82.13% reduction. The results indicate that the TMPD has better performance than the conventional PD under this excitation level. Recalling the nonlinear relation between the excitation level and the responses, we further compare the peak response amplitudes of all the four configurations when they are subjected to a series of excitation levels. For the primary structure integrated with the TMPD, both the first mode and the second are analyzed as the TMPD adds an additional DOFs to the system. We take into account that the particle motions will change the peak response frequencies of the system, and let the ranges of excitation frequency be 5.66–5.93 Hz (for the first mode) and 9.94–10.31 Hz (for the second mode). Here, 5.66 Hz and 9.94 Hz are the first and second natural frequencies of the integrated system when all the particles are fixed to the enclosure floor, and 5.93 Hz and 10.31 Hz are those when all the particles are not in contact with the enclosure. The actual peak responses will occur within these frequency ranges. Without loss of generality, the excitation level is set to be from 0.01 N to 0.16 N with an interval step of 0.01 N and from 0.18 N to 0.30 N with interval step of 0.02 N. The ratio of the RMS value of the peak response amplitudes of the primary structure without any damper to that with various damping devices, σ_{r0}/σ_r, is used to quantify the vibration suppression effectiveness for each configuration.

Figure 11 shows the results of peak responses (within the aforementioned frequency ranges) of all the four configurations versus excitation levels. The ratio is one for the baseline configuration (1). It can be observed that the TMPD consistently outperforms the conventional PD as well as the undamped absorber. When the excitation level is lower than 0.05 N, the conventional PD has little damping effect, since the gravity essentially locks the particles together to rest on the floor of the enclosure. The TMPD, in contrast, exhibits noticeable vibration suppression capability for both the first and second resonances even when the excitation force amplitude is at 0.03 N, owing to its motion magnifying effect that can amplify the particle acceleration to above gravity. This demonstrates the effectiveness of the TMPD at very low level vibrations of the primary structure.

For the conventional PD, as the excitation level increases to above 0.05 N, the particles begin to slide over and collide with each other, producing more significant damping effect via momentum exchange and internal energy dissipation. Eventually, the PD reaches its maximum damping capacity at excitation amplitude of 0.11 N, as illustrated in Fig. 11. Although further increase of excitation amplitude yields more drastic particle motions, the energy dissipation capacity appears to saturate and the peak response reduction actually decreases. Compared with the conventional PD, the vibration suppression performance of TMPD is much better, as shown in Fig. 11, yielding as much as 9.37 times more response reduction (for the second resonance). First and foremost, the motions of the particles in the TMPD are greatly amplified, resulting in more significant momentum exchange between the particles and the enclosure as well as greater energy dissipation inside the enclosure. Second, the TMPD acts also as an undamped vibration absorber that can store

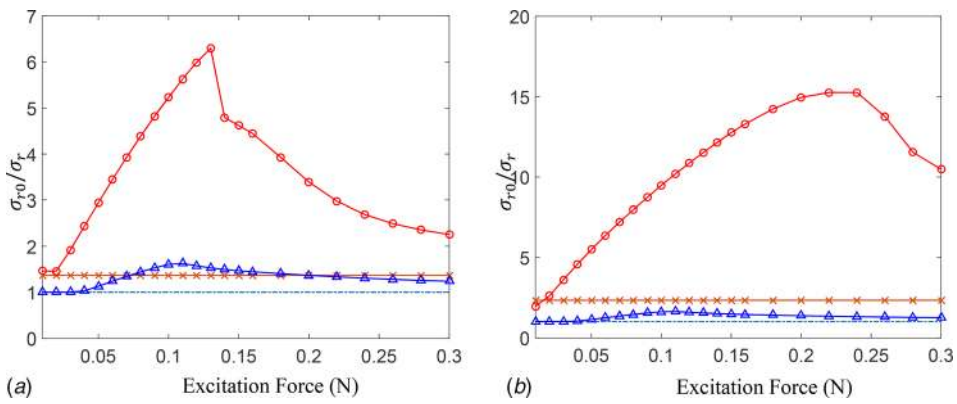

Fig. 11 Comparison of vibration suppression performances of four configurations under different excitation levels. –·–·–: Configuration 1 (baseline); —△—: configuration 2 (PD); —×—: configuration 3 (undamped absorber); and —□—: configuration 4 (TMPD). (*a*) first mode and (*b*) second mode.

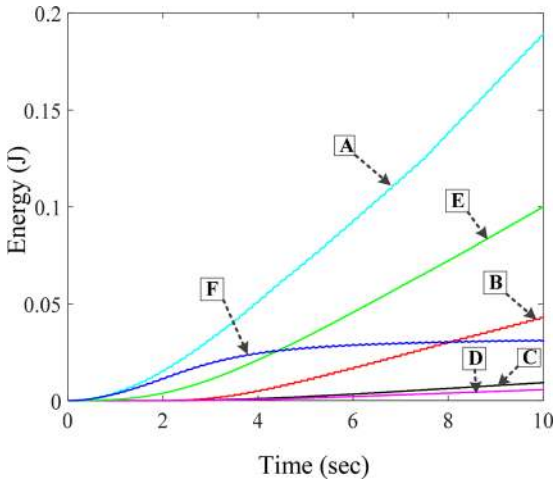

Fig. 12 Cumulative energies ($A = 0.11$ N) under the PD: (A) work done by external force, (B) interparticle interaction, (C) particle-to-ceiling/floor impact, (D) particle-to-wall friction, (E) inherent damping dissipation, and (F) remaining energy of the primary structure

a significant portion of the vibratory energy. Although the main purpose for us to involve the undamped absorber (configuration (3)) in this analysis is to analyze the damping mechanisms of the TMPD, the undamped absorber itself can be used to suppress vibration. It is well known that an undamped absorber may suppress vibration through absorbing a portion of the vibratory energy from the host structure (while an additional degrees-of-freedom is added to the primary structure so the response characteristics are changed). For instance, for the first resonant peak (Fig. 11(*a*)), the undamped absorber (configuration (3)) has a better vibration suppression effect than the PD when the excitation level is below 0.07 N and above 0.20 N; for the second resonant peak (Fig. 11(*b*)), the vibration suppression effect of the undamped absorber (configuration (3)) is higher than the PD for the entire frequency range. Owing to the two combinatorial effects of increased damping and vibration absorption, the TMPD can reduce the resonant peak responses drastically. Meanwhile, it can be observed that the excitation level still affects the vibration reduction capability of TMPD. As the excitation level increases, the vibration suppression effect of the TMPD for the first resonance increases before it reaches 0.13 N, and that of the TMPD for the second resonance increases before it reaches 0.24 N. If the excitation level increases further, the respective peak responses will start to increase again.

We then analyze the energy dissipation mechanisms. In particle damping, the energy dissipation is mainly due to interparticle interaction, particle-to-ceiling/floor impact, and particle-to-wall friction. To further compare the damping effect of TMPD and PD, we calculate the individual energy dissipation for the case of $A = 0.11$ N during the first 10 s, where the excitation frequencies are $f_1 = 7.15$ Hz (i.e., the first and only peak response frequency) for the PD case and $f_2 = 5.70$ Hz and $f_3 = 10.00$ Hz (i.e., the first and second peak response frequencies) for the TMPD case, respectively. For the PD, Fig. 12 shows that under this excitation level, the inherent structural damping dominates the energy dissipation as compared with the particle damping, even though the PD has already reached its apparent optimal status in terms of excitation level (see Fig. 11). The particles start to dissipate system energy noticeably after 3 s, but the remaining energy of the steady-state vibrating primary system is still large relative to the total work done by the external excitation. In contrast, for the TMPD, it can be observed from Figs. 13(*a*) and 13(*b*) that the interparticle interaction contributes significantly to the overall damping for both the first and second response peaks, and particles can quickly start to dissipate the system energy (before 2 s) due to the motion magnifying effect of TMPD. This results in a considerably lower remaining energy of the primary structure. It

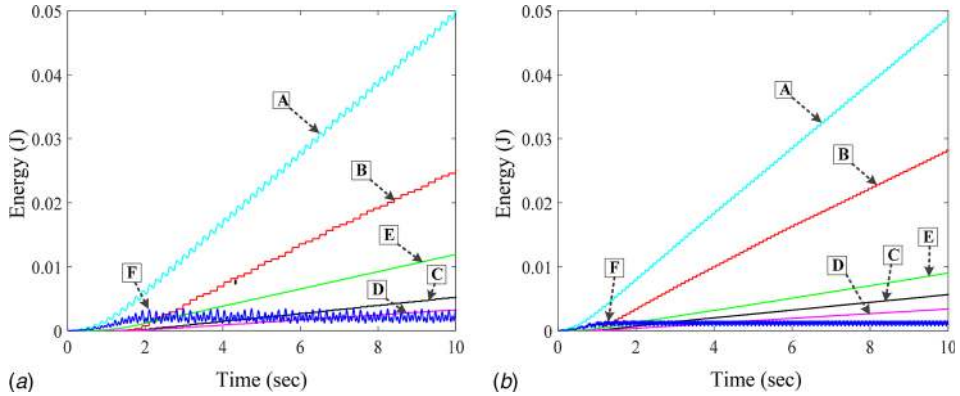

Fig. 13 Cumulative energies ($A = 0.11$ N) under the TMPD: (A) work done by external forces, (B) interparticle interaction, (C) particle-to-ceiling/floor impact, (D) particle-to-wall friction, (E) inherent damping dissipation, and (F) remaining energy of the primary structure. (*a*) First mode and (*b*) second mode.

Table 3 Comparison of energy dissipations of PD and TMPD

	PD			TMPD (mode 1)			TMPD (mode 2)		
A (N)	WE (J)	RE (J)	RE/WE	WE (J)	RE (J)	RE/WE	WE (J)	RE (J)	RE/WE
0.08	0.107	0.0209	0.195	0.0318	0.00261	0.0821	0.0295	0.000970	0.0329
0.11	0.190	0.0309	0.163	0.0500	0.00331	0.0662	0.0487	0.00104	0.0214
0.13	0.263	0.0457	0.174	0.0673	0.00346	0.0514	0.0652	0.00111	0.0170
0.24	0.928	0.198	0.213	0.273	0.0246	0.0901	0.177	0.00209	0.0118
0.30	1.50	0.340	0.227	0.490	0.0557	0.114	0.284	0.00538	0.0189

Note: WE: work done by external force and RE: remaining energy of the primary structure.

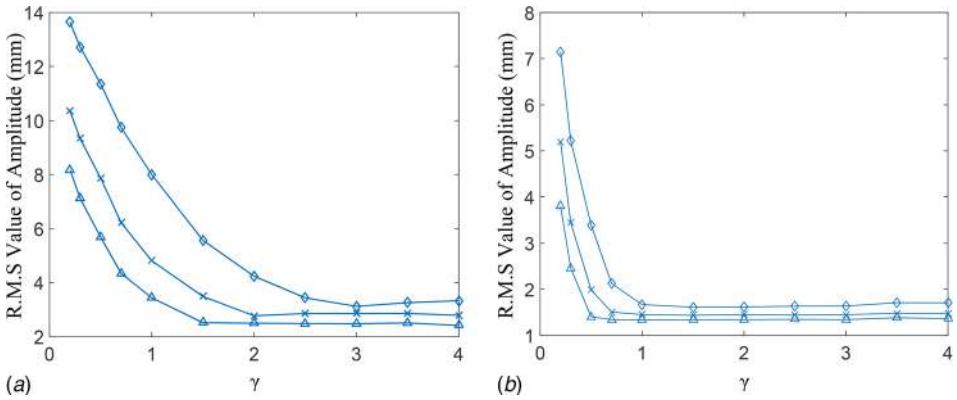

Fig. 14 Influence of enclosure geometry to the damping effect of TMPD under different excitation levels. : 0.20 N; : 0.24 N; and : 0.30 N. (*a*) First mode and (*b*) second mode.

Table 4 Damping performance of TMPD under different enclosure geometries

	Mode 1			Mode 2		
γ	1.0	2.0	3.0	0.5	1.0	2.0
RE/WE	0.0160	0.0044	0.0036	0.0115	0.0065	0.0078

Note: WE: work done by external force and RE: remaining energy of the primary structure.

is worth noting that, for both resonant peak responses, under the excitation level of $A = 0.11$ N, the TMPD does not even reach the apparent optimal operating condition (see Fig. 11).

We further vary the excitation amplitudes and examine the corresponding energy dissipations of the TMPD and the PD. For each excitation amplitude, we search for the respective response peaks of the PD and the TMPD. We compare the total work done by the external excitation forces, the remaining energy of the primary structure, and the ratio of the remaining energy of the primary structure to the total external work done, under the resonant peak frequencies, which are listed in Table 3. Apparently, the lowest ratio of the remaining energy and the total work done for the PD and the lowest ratios of the first and second peak for the TMPD are reached when the excitation amplitudes are 0.11 N, 0.13 N, and 0.24 N, respectively. These are consistent with the results shown in Fig. 11. The particles indeed dissipate more energy when the excitation level is high. The remaining energy of the primary structure, however, may still be high since the absolute levels of response may also be high as excitation level increases.

4.2 Parametric Influence to TMPD Performance. Using numerical simulation, we can explore the influence of some design parameters to the vibration suppression performance of the TMPD. We first investigate the enclosure geometry. The volume and width of the enclosure as well as all the other parameters are kept constant (i.e., the same as those listed in Tables 1 and 2), and we only change the ratio of the enclosure height to length, denoted by γ. This affects how the particles impact the enclosure ceiling. Again, we search for the response peaks for the first and second modes of the integrated system under each γ ratio. Figures 14(*a*) and 14(*b*) show the results under different excitation levels 0.20 N, 0.24 N, and 0.30 N, respectively. As can be seen, for small ratio γ, the amplitudes of both the first and second resonant response peaks are relatively high for all the excitation levels applied. The reason is that, when the clearance height is small, many particles only have limited motion and also impact frequently with the enclosure floor/ceiling, so they behave more like added-on mass to the system. As the ratio increases, the energy dissipation effect of the TMPD increases and reaches certain optimal value. If the ratio further increases, the energy dissipation effect saturates since particles will not be able to reach the enclosure ceiling. The frequencies of the peak responses of the system under different ratios γ indeed change, i.e., 5.66 Hz, 5.69 Hz, and 5.75 Hz under ratio $\gamma = 1.0$, 2.0, and 3.0, respectively, for the first mode when the excitation amplitude is 0.24 N. The ratios of the remaining energy to the total work done by the external force, for the first and second modes, are listed in Table 4. It can be observed that the energy ratios are consistent with the results shown in Fig. 14.

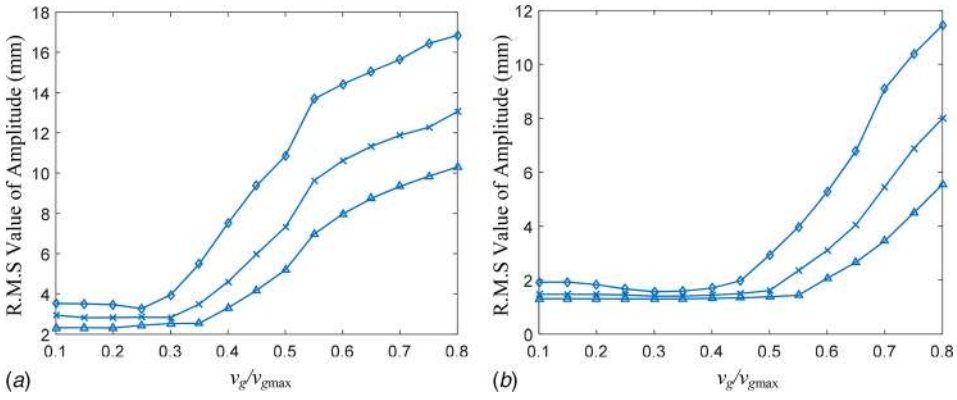

Fig. 15 Influence of volumetric filling ratio to the damping performance of TMPD under different excitation levels. : 0.20 N; : 0.24 N; and : 0.30 N. (*a*) First mode and (*b*) second mode.

We also investigate the particle volumetric filling ratio v_g that is defined as the ratio of the volume occupied by the particles to the volume of the enclosure for the TMPD. Here, the change of v_g is facilitated by varying the height of the enclosure only. Similarly, we search for the response peak amplitudes for the first and the second modes. Figures 15(*a*) and 15(*b*) illustrate the influence of the particle volumetric filling ratio to the peak responses. The excitation levels used in this analysis are 0.20 N, 0.24 N, and 0.30 N, respectively. For the first resonant peak, as the volumetric filling ratio increases after certain value of $v_g/v_{g\max}$ where $v_{g\max}$ is the maximum volumetric filling ratio, the vibration suppression performance goes down. Before that, it is actually insensitive to the volumetric filling ratio as particles may not reach the enclosure ceiling. It can be observed that the critical volumetric filling ratio will decrease as the excitation levels increase, since the under increased excitation levels the particles are able to impact the ceiling more easily. A similar observation can be reached for the second resonant peak, where the critical ratios are $v_g/v_{g\max} = 0.55$, 0.5, and 0.4 for excitation levels of 0.20 N, 0.24 N, and 0.30 N, respectively, beyond which the vibration suppression performance goes down. From these results, we can conclude that while the volumetric filling ratio is an important parameter, there exists a range within which the TMPD performs in a fairly robust manner.

5 Conclusion

In this research, we investigate systemically the integration of particle damping mechanism into the tuned mass damper configuration which forms the TMPD. The TMPD does not employ viscous or hysteretic materials and therefore can be used in harsh environments especially under high temperature. The vibration response characteristics of a benchmark beam structure integrated with TMPD are analyzed by combining beam dynamic analysis with discrete element-based particle motion analysis. Our analysis indicates that the TMPD can effectively magnify the particle motion, thereby enhancing remarkably the energy dissipation capacity of the particles especially under low vibration scenarios. With the combinatorial effects of the increased energy dissipation and the vibration absorption, the TMPD exhibits significantly enhanced vibration suppression capability than conventional particle damper.

Acknowledgment

This research was supported in part by the NSF under Grant No. CMMI-1130724.

References

[1] Jones, D. I., 2001, *Handbook of Viscoelastic Vibration Damping*, Wiley, Chichester, UK.
[2] Friend, R. D., and Kinra, V. K., 2000, "Particle Impact Damping," J. Sound Vib., **233**(1), pp. 93–118.
[3] Saeki, M., 2002, "Impact Damping With Granular Materials in a Horizontally Vibrating System," J. Sound Vib., **251**(1), pp. 153–161.
[4] Mao, K., Wang, M. Y., Xu, Z., and Chen, T., 2004, "DEM Simulation of Particle Damping," Powder Technol., **142**(2), pp. 154–165.
[5] Saeki, M., 2005, "Analytical Study of Multi-Particle Damping," J. Sound Vib., **281**(3), pp. 1133–1144.
[6] Gharib, M., and Karkoub, M., 2015, "Shock-Based Experimental Investigation of the Linear Particle Chain Impact Damper," ASME J. Vib. Acoust., **137**(6), p. 061012.
[7] Wu, C. J., Liao, W. H., and Wang, M. Y., 2004, "Modeling of Granular Particle Damping Using Multiphase Flow Theory of Gas-Particle," ASME J. Vib. Acoust., **126**(2), pp. 196–201.
[8] Xu, Z. W., Chan, K., and Liao, W., 2004, "An Empirical Method for Particle Damping Design," Shock Vib., **11**(5–6), pp. 647–664.
[9] Fang, X., and Tang, J., 2006, "Granular Damping in Forced Vibration: Qualitative and Quantitative Analyses," ASME J. Vib. Acoust., **128**(4), pp. 489–500.
[10] Tijskens, E., Ramon, H., and Baerdemaeker, J. D., 2003, "Discrete Element Modelling for Process Simulation in Agriculture," J. Sound Vib., **266**(3), pp. 493–514.
[11] Mao, K., Wang, M. Y., Xu, Z., and Chen, T., 2004, "Simulation and Characterization of Particle Damping in Transient Vibrations," ASME J. Vib. Acoust., **126**(2), pp. 202–211.
[12] Fang, X., Tang, J., and Luo, H., 2007, "Granular Damping Analysis Using an Improved Discrete Element Approach," J. Sound Vib., **308**(1), pp. 112–131.
[13] Cundall, P. A., and Strack, O. D., 1979, "A Discrete Numerical Model for Granular Assemblies," Geotechnique, **29**(1), pp. 47–65.
[14] Lu, Z., Masri, S. F., and Lu, X., 2011, "Parametric Studies of the Performance of Particle Dampers Under Harmonic Excitation," Struct. Control Health Monit., **18**(1), pp. 79–98.
[15] Salueña, C., Pöschel, T., and Esipov, S. E., 1999, "Dissipative Properties of Vibrated Granular Materials," Phys. Rev. E, **59**(4), p. 4422.
[16] Liu, W., Tomlinson, G., and Rongong, J., 2005, "The Dynamic Characterisation of Disk Geometry Particle Dampers," J. Sound Vib., **280**(3), pp. 849–861.
[17] Yao, B., Chen, Q., Xiang, H., and Gao, X., 2014, "Experimental and Theoretical Investigation on Dynamic Properties of Tuned Particle Damper," Int. J. Mech. Sci., **80**, pp. 122–130.
[18] Sun, J. Q., Jolly, M. R., and Norris, M. A., 1995, "Passive, Adaptive and Active Tuned Vibration Absorbers—A Survey," ASME J. Mech. Des., **117**(B), pp. 234–242.
[19] Zuo, L., and Nayfeh, S. A., 2004, "Minimax Optimization of Multi-Degree-of-Freedom Tuned-Mass Dampers," J. Sound Vib., **272**(3), pp. 893–908.
[20] Febbo, M., and Vera, S., 2008, "Optimization of a Two Degree of Freedom System Acting as a Dynamic Vibration Absorber," ASME J. Vib. Acoust., **130**(1), p. 011013.
[21] Yang, C., Li, D., and Cheng, L., 2011, "Dynamic Vibration Absorbers for Vibration Control Within a Frequency Band," J. Sound Vib., **330**(8), pp. 1582–1598.
[22] Simonian, S., and Brenana, S., 2006, "Tunable Adjustable Multi-Element Hybrid Particle Damper," U.S. Patent Application No. 11/375, 716.
[23] Ou, Q., Chen, X., Gutschmidt, S., Wood, A., Leigh, N., and Arrieta, A. F., 2012, "An Experimentally Validated Double-Mass Piezoelectric Cantilever Model for Broadband Vibration-Based Energy Harvesting," J. Intell. Mater. Syst. Struct., **23**(2), pp. 117–126.
[24] Tsuji, Y., Tanaka, T., and Ishida, T., 1992, "Lagrangian Numerical Simulation of Plug Flow of Cohesionless Particles in a Horizontal Pipe," Powder Technol., **71**(3), pp. 239–250.
[25] Zhang, D., and Whiten, W., 1996, "The Calculation of Contact Forces Between Particles Using Spring and Damping Models," Powder Technol., **88**(1), pp. 59–64.
[26] Mishra, B., and Murty, C., 2001, "On the Determination of Contact Parameters for Realistic DEM Simulations of Ball Mills," Powder Technol., **115**(3), pp. 290–297.
[27] Johnson, K. L., 1985, *Contact Mechanics*, Cambridge University Press, Cambridge, UK.
[28] Verlet, L., 1967, "Computer 'Experiments' on Classical Fluids—I: Thermodynamical Properties of Lennard-Jones Molecules," Phys. Rev., **159**(1), p. 98.
[29] Zhou, W., Penamalli, G. R., and Zuo, L., 2012, "An Efficient Vibration Energy Harvester With a Multi-Mode Dynamic Magnifier," Smart Mater. Struct., **21**(1), p. 015014.